Article

Doping Shortens the Metal/Metal Distance and Promotes OH Coverage in Non-Noble Acidic Oxygen Evolution Reaction Catalysts

Ning Wang,[†] Pengfei Ou,[†] Rui Kai Miao,[†] Yuxin Chang,[†] Ziyun Wang,[†] Sung-Fu Hung, Jehad Abed, Adnan Ozden, Hsuan-Yu Chen, Heng-Liang Wu, Jianan Erick Huang, Daojin Zhou, Weiyan Ni, Lizhou Fan, Yu Yan, Tao Peng, David Sinton, Yongchang Liu, Hongyan Liang,* and Edward H. Sargent*

Read Online

ACCESS | Metrics & More | Article Recommendations | Supporting Information

ABSTRACT: Acidic water electrolysis enables the production of hydrogen for use as a chemical and as a fuel. The acidic environment hinders water electrolysis on non-noble catalysts, a result of the sluggish kinetics associated with the adsorbate evolution mechanism, reliant as it is on four concerted proton-electron transfer steps. Enabling a faster mechanism with non-noble catalysts will help to further advance acidic water electrolysis. Here, we report evidence that doping Ba cations into a Co_3O_4 framework to form $Co_{3-x}Ba_xO_4$ promotes the oxide path mechanism and simultaneously improves activity in acidic electrolytes. $Co_{3-x}Ba_xO_4$ catalysts reported herein exhibit an overpotential of 278 mV at 10 mA/cm^2 in 0.5 M H_2SO_4 electrolyte and are stable over 110 h of continuous water oxidation operation. We find that the incorporation of Ba cations shortens the Co—Co distance and promotes OH adsorption, findings we link to improved water oxidation in acidic electrolyte.
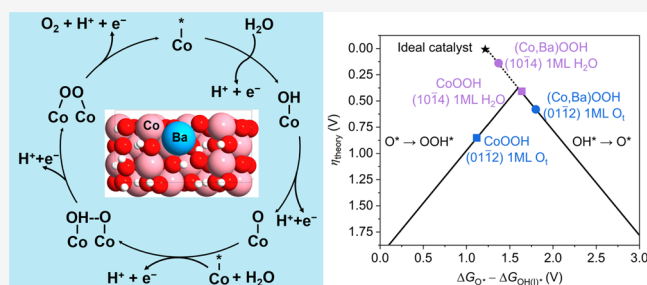
INTRODUCTION

In water electrolysis for renewable hydrogen production, acidic electrolyzers provide advantages—when compared with conventional alkaline water electrolyzers—that include a compact cell size, low ohmic loss, and high current densities and efficiencies.[1−3] However, the corrosive acidic environment of a water electrolyzer at pH = ~0 has, to date, required noble metal catalysts for the oxygen evolution reaction (OER), raising concerns around the long-term roadmap to scale.[4,5] Noble-metal-free OER catalysts that combine high catalytic activity with the needed resistance to corrosion will contribute toward the success of acidic water electrolysis.

Strategies to improve catalytic performance and stability[6−9] have made great strides; yet, to date, the resultant catalysts have exhibited poor stability in acidic electrolytes; none has yet proven competitive with Ir-based catalysts.[10,11]

The oxide path mechanism (OPM) in the OER,[12−14] which allows direct O—O radical coupling with the absence of oxygen vacancy defects, is seen in the Co_3O_4 system in alkaline and neutral media.[15,16] However, when utilized in acidic conditions,[17−20] the Co_3O_4 family relies on an adsorbate evolution mechanism (AEM),[21,22] which involves multiple oxygen reaction intermediates and exhibits more sluggish catalytic performance as well as limited stability.

Here, we sought to dope Ba into Co_3O_4 to modify the Co—Co distance and intermediate coverage, a concept that we believed had the potential to activate the OPM pathway,

something that could increase activity in acidic electrolytes. From density functional theory (DFT) studies, we conclude that the surface-adsorbed Ba atoms lower the surface free energy of stable surfaces of CoOOH and enhance its stability in acidic electrolyte. In situ measurements that probe changes in the reaction intermediates provide indications of the OPM pathway. We develop $Co_{3-x}Ba_xO_4$ catalysts having an over-potential of 278 mV at 10 mA/cm^2 and 110 h of continuous operation in 0.5 M H_2SO_4 electrolyte.

RESULTS AND DISCUSSION

Synthesis and Activity of Co_3O_4 Catalysts and the Ba-Dopant Effect. We began with the synthesis of Co_3O_4 catalysts via an electrodeposition method and tested OER performance in 0.5 M H_2SO_4 electrolyte (pH = 0.3) (see the Materials and Methods section). Linear sweep voltammetry (LSV) and chronopotentiometry curves show that the activity and stability match previously reported performance,[23] but we find that the performance resides below that of noble-metal-based catalysts (Figures S1 and S2). Since Ba doping has been

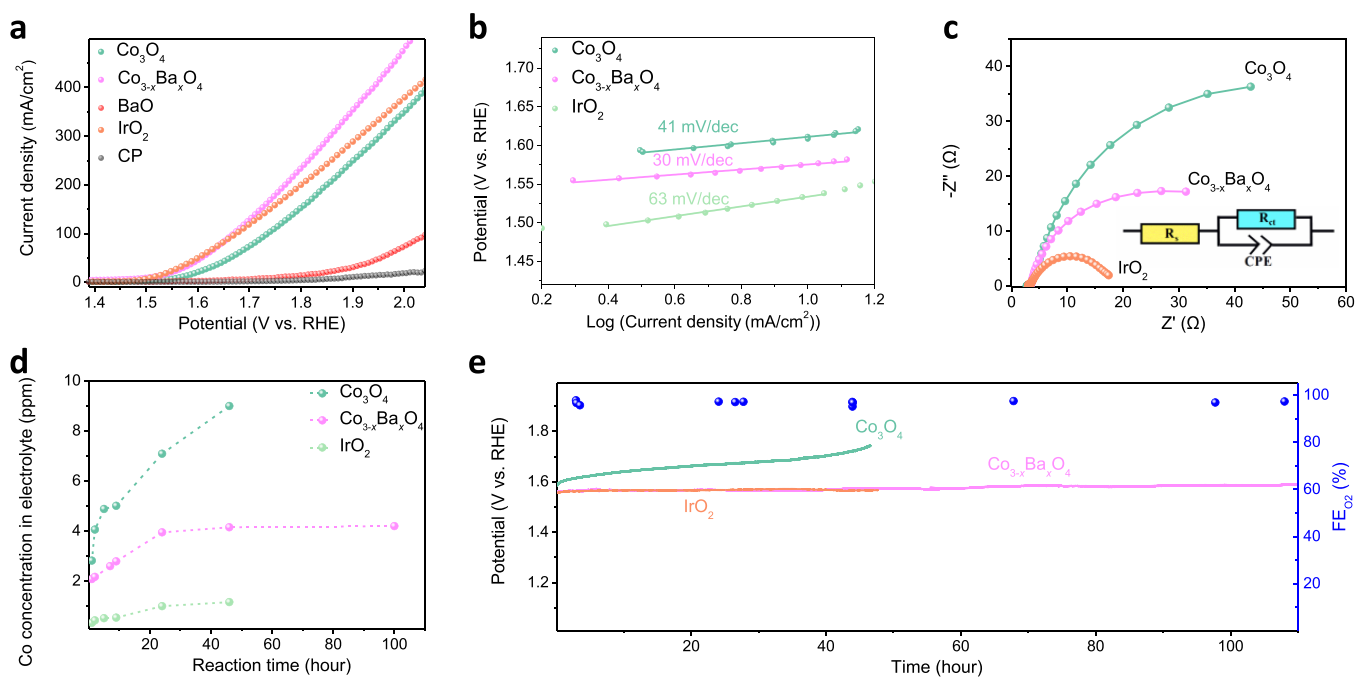**Figure 1.** Catalytic performance of $Co_{3-x}Ba_xO_4$ and controls. (a) LSV curves at a 5 mV/s scan rate without iR correction for $Co_{3-x}Ba_xO_4$ and control catalysts deposited onto carbon paper substrates in 0.5 M H_2SO_4 electrolyte. (b) Tafel slope curves. (c) EIS data collected for the electrodes under 1.5 V vs RHE. The inset provides the equivalent circuit: R_s, series resistance; R_{ct}, charge-transfer resistance; CPE, constant-phase element related to the double-layer capacitance. (d) ICP concentrations of Co or Ir vs reaction time for $Co_{3-x}Ba_xO_4$ and control catalysts. We took out 1 mL from 35 mL testing electrolyte during the stability and diluted it to 10 mL in a separate centrifuge tube to test the concentration. (e) Chronopotentiometry curves obtained from catalysts at a constant current density of 10 mA/cm² in single cells, and the corresponding Faradaic efficiencies of the evolved O_2 from gas chromatography measurements for the $Co_{3-x}Ba_xO_4$ catalyst.

seen to increase activity and stability in acidic systems,[24] we synthesized $Co_{3-x}Ba_xO_4$ and investigated the effects of the Ba dopant on the electronic structure, catalytic performance, and mechanism.

The $Co_{3-x}Ba_xO_4$ catalysts were electrodeposited on carbon paper substrates using the same method as for the Co_3O_4 catalysts. The inductively coupled plasma optical emission spectroscopy (ICP-OES) result shows that the Ba atomic ratio is 8%. Then, we characterized its electrocatalytic performance in acidic electrolyte. LSV (Figure 1a) and cyclic voltammetry (Figure S3) polarization measurements indicate that the overpotential at 10 mA/cm² is 278 ± 3 mV, ~70 mV lower than that for the Co_3O_4 catalysts (Figure S4). The $Co_{3-x}Ba_xO_4$ OER catalyst also showed high catalytic performance in 1 M KOH electrolyte (Figure S5). Catalytic activity comparisons were made using chronoamperometry and polarization plots (Figure S6). We obtained similar results: $Co_{3-x}Ba_xO_4$ shows the best catalytic performance with increased applied potential. Optimizing the concentration of Ba enables a further improvement in catalytic performance (Figure S7). $Co_{3-x}Ba_xO_4$ outperforms previously reported acidic noble-metal-free OER electrocatalysts (Table S1).

We then turned to study performance and stability when 1 M $HClO_4$ is used as the electrolyte (Figure S8). This would allow us to check for the possibility that performance improvement had arisen due to the formation of $BaSO_4$. $Co_{3-x}Ba_xO_4$ outperforms Co_3O_4 catalysts, indicating that $BaSO_4$ formation is not the main reason underlying the performance improvement. The lower Tafel slope compared to the Co_3O_4 catalyst shows that the $Co_{3-x}Ba_xO_4$ catalyst enables faster reaction kinetics compared to the Co_3O_4 catalyst (Figure 1b). The electrochemical impedance spectroscopy curve (EIS,

Figure 1c and Table S2) shows that the incorporation of Ba decreases the charge-transfer resistance (R_{ct}, 384 → 45 Ω).

To evaluate intrinsic catalytic activity, we further took advantage of the electrochemically active surface area (ECSA) to normalize the current density (Figures S9 and S10). Normalized results show that the current density of the $Co_{3-x}Ba_xO_4$ catalyst is 3× greater than the value of Co_3O_4, 4.2× higher than the value of the IrO_2 control catalyst at 1.7 V vs RHE. We also evaluated the iR-corrected LSV curves to check for any effects from cell geometry and conductivity on performance (Figure S11). The $Co_{3-x}Ba_xO_4$ catalyst presents the highest iR-corrected current density at 1.63 V vs RHE, nearly 5.7× higher than that of the Co_3O_4 catalyst and 1.8× higher than that of the IrO_2 catalyst. The turnover frequency (TOF, Table S3) analysis demonstrated the same trend: the $Co_{3-x}Ba_xO_4$ catalyst exhibits the fastest TOF of 0.96 s⁻¹, which is 2.7× and 1.6× faster than the values of Co_3O_4 and IrO_2 catalysts, respectively.

We tested the operating acidic stability of $Co_{3-x}Ba_xO_4$ and control catalysts at 10 mA/cm² and tested the Co concentration in the electrolyte at different reaction times. The ICP results showed that the addition of Ba cations suppresses the Co leaching rate, enabling leaching rates near to those seen in Ir-based catalysts (Figures 1d and S12). Additionally, $Co_{3-x}Ba_xO_4$ catalysts retained an overpotential to 280 mV following 110 h of continuous water splitting, superior to control catalysts (Figure 1e). The Faradaic efficiency (FE) toward oxygen production remained at 99% throughout, indicating that the OER dominates the overall reaction rather than material corrosion. Surface transmission electron microscopy and scanning electron microscopy images show that the catalyst maintains its morphological and
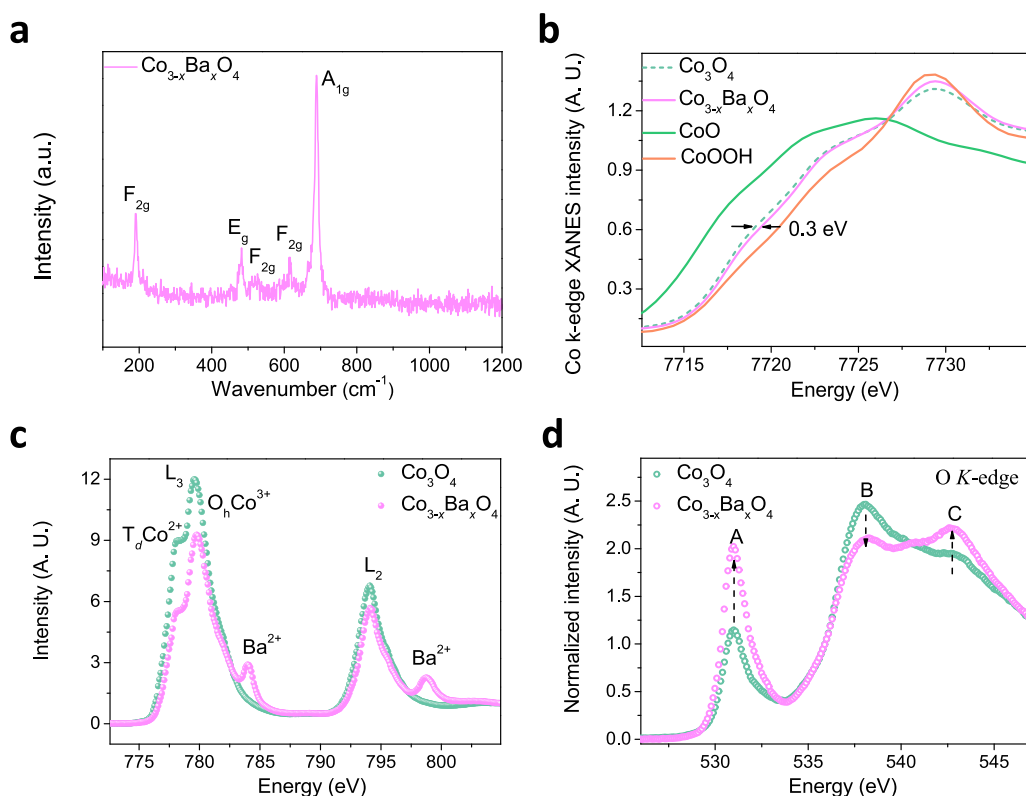
Figure 2. Electronic structure characterization of the $Co_{3-x}Ba_xO_4$ catalyst and controls. (a) Raman spectrum of the $Co_{3-x}Ba_xO_4$ catalyst. Its five characteristic peaks similar to Co_3O_4. (b) Co K-edge XANES spectra at 1.6 V vs RHE. (c) Co L-edge, it can be split into two separate sets of peaks named L_3 and L_2-edges as a result of the 2p spin-orbital coupling interaction. (d) O K-edge XAS curves of catalysts.
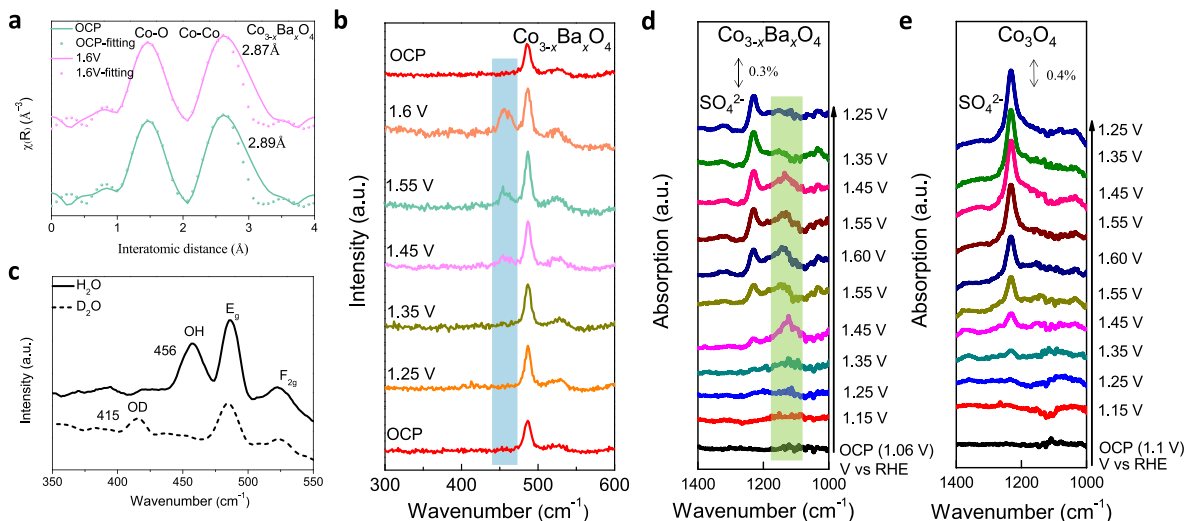

Figure 3. Mechanistic investigations of the $Co_{3-x}Ba_xO_4$ catalysts for acidic electrochemical water oxidation. (a) In situ extended X-ray absorption fine structure spectra of the Co K-edge from $Co_{3-x}Ba_xO_4$ at OCP and 1.6 V vs RHE. The peak at 1.0−2.0 Å corresponds to the distance of Co−O bonds. The peak at 2.0−3.0 Å corresponds to the Co−Co distance. (b) In situ Raman spectra of the $Co_{3-x}Ba_xO_4$ catalyst on a carbon paper substrate in 0.5 M H_2SO_4 electrolyte. (c) Raman peak comparison in 0.5 M H_2SO_4 + D_2O/H_2O electrolyte. FTIR spectra recorded in the potential range of OCP to 1.6 V versus RHE for (d) $Co_{3-x}Ba_xO_4$ and (e) Co_3O_4.

compositional features after the stability test (Figures S13–S16). X-ray photoelectron spectroscopy (XPS) measurements suggest that the catalyst maintains compositional features throughout the stability test (Figure S17). The similarity in Ba atomic ratios before (ICP 8%) and after (ICP 10%) the stability test suggests high corrosion resistance of $Co_{3-x}Ba_xO_4$ in acidic electrolytes.

Catalyst Structure Characterization. We turned to investigate the structure of $Co_{3-x}Ba_xO_4$. XPS and L_3-edge X-ray absorption spectroscopy (XAS) spectra indicate Ba existence in the $Co_{3-x}Ba_xO_4$ catalysts (Figures S18 and 19). Lattice fringe images show that the Ba-doped catalyst shows a shortened lattice distance value compared to the Co_3O_4 catalyst, consistent with the Rietveld X-ray diffraction (XRD)
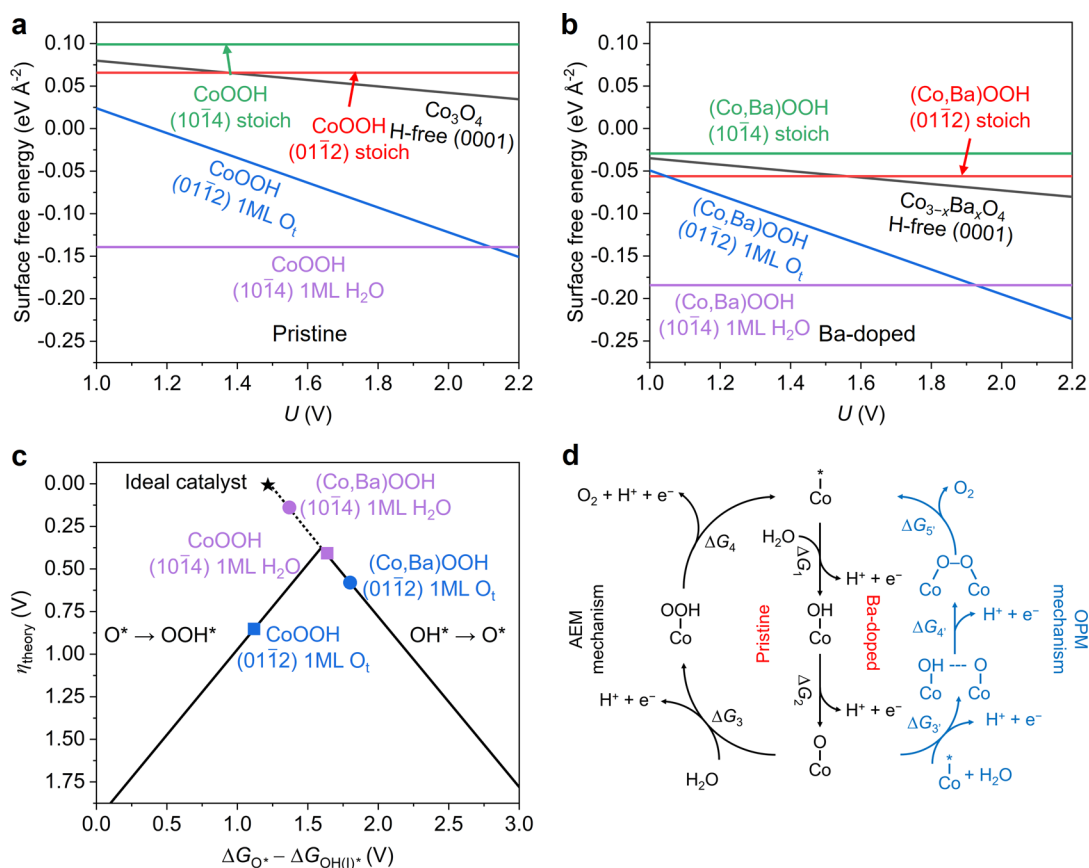
Figure 4. Comparison of surface stability and OER energetics between pristine and Ba-doped surfaces. (a) Surface free energy for different slabs of pristine Co_3O_4 and CoOOH as a function of applied potential at pH = 0, including the H-free (0001) surface of Co_3O_4(0001), $(01\bar{1}2)$ surfaces with stoichiometry (stoich) and with 1 ML O_t, and $(10\bar{1}4)$ surfaces with stoichiometry (stoich) and with 1 ML coadsorbed H_2O of CoOOH, respectively. (b) Surface free energy for different slabs of Ba-doped Co_3O_4 and CoOOH as a function of applied potential at pH = 0, including the H-free (0001) surface of $Co_{3-x}Ba_xO_4$, $(01\bar{1}2)$ surfaces with stoichiometry and with 1 ML O_t as well as $(10\bar{1}4)$ with stoichiometry and with 1 ML coadsorbed H_2O of (Co,Ba)OOH, respectively. (c) OER volcano plot showing the predicted theoretical overpotential (η_{theory}, V) versus the free energy difference between the formation of O* and OH* ($\Delta G_{O*} - \Delta G_{OH(I)*}$, eV). $\Delta G_{OH(I)*}$ denotes the free energy for the formation of first OH* in the OPM mechanism, whereas for OH* formation in the AEM. (d) OPM (dual O—O coupling) vs AEM (conventional) OER mechanism for catalysts in acidic electrolyte.

refinement analysis (Figures S20–21 and Table S4). Similar Raman spectra of $Co_{3-x}Ba_xO_4$ and Co_3O_4 argued against Ba phase segregation (Figure 2a). The Raman spectrum of the $Co_{3-x}Ba_xO_4$ catalyst underwent a blue-shift, consistent with the shortened Co—O and Co—Co distance. The FWHM values are 20 and 18.3 for Co_3O_4 and $Co_{3-x}Ba_xO_4$ catalysts (Figure S22).

Next, we investigated the effects of Ba doping on the electronic structure. Using in situ XAS, we found that, following Ba doping, the K-edge X-ray absorption near-edge structure (XANES, Figure 2b) curves of Co show a positive edge-shift, suggesting a higher Co valence state in $Co_{3-x}Ba_xO_4$ catalysts. Symmetry analysis on the edge feature of XANES shows that the pre-edge intensity for the $Co_{3-x}Ba_xO_4$ catalyst is higher than that for Co_3O_4, suggesting that the insertion of Ba ions into the Co_3O_4 lattice reduces the local geometry of the cobalt ions (Figure S23). Since the 3d electrons of Co ions participate in the catalytic process of the OER, the electronic structure of the 3d orbital dictates the overall catalytic behavior.[25] We conducted Co L-edge XAS (2p-3d) to analyze the effect of the Ba dopant on the d-orbital structure.[25] As shown in Figure 2c, we detected a similar trend: Ba doping increases the Co oxidation state. Previous studies have

illustrated that transition metal active sites with high valence promote OER performance.[26–28]

To explore further the origins of high-valence active sites, we characterized the O K-edge XANES spectra for $Co_{3-x}Ba_xO_4$ and the control catalyst (Figure 2d). Both normalized spectra have three main features labeled A, B, and C. We examined an increase in intensity in region A when doping with Ba, a spectral feature that indicates a higher concentration of Co^{3+},[29] consistent with Co L-edge results. The decrease in peak B and increase in peak C indicate an increased disorder of the outer oxygen shell and interaction between the first oxygen shell and Co:[30] we offer that the latter may foster the formation of high-valence Co.

In Situ Studies for Mechanistic Investigations. We studied the effects of Ba cations on the local bonding environment of Co using the extended X-ray absorption fine structure spectrum (EXAFS). By analyzing the fitting results at open-circuit potential (OCP) and 1.6 V vs RHE of $Co_{3-x}Ba_xO_4$ catalysts (Figure 3a and Table S5), we obtained a shorter Co—Co distance under OER conditions than OCP (2.89 → 2.87 Å). We also compared the Co—Co distance of Co_3O_4 catalysts and observed similar distance values under OCP and OER potential (Figure S24). These results indicate

that the $Co_{3-x}Ba_xO_4$ catalyst shows a shorter Co−Co distance under applied potential.

A series of in situ Raman experiments were conducted to analyze the OER potential-resolved intermediate variation on $Co_{3-x}Ba_xO_4$ and Co_3O_4 surfaces (Figure 3b and S25−S26). At the OCP, both Co_3O_4 and $Co_{3-x}Ba_xO_4$ samples present four Raman characteristic peaks.[12] Under positive potential sweeping, a peak at 456 cm^{-1} emerged on the $Co_{3-x}Ba_xO_4$ surface at 1.45 V vs RHE, attributing to the OH group formation on the catalyst surface.[31] Further Raman test showed that a new peak was more clearly detected at 1.6 V vs RHE and disappeared when the potential backed to the OCP. To exclude the byproduct interference, we compared these Raman peaks in D_2O and H_2O electrolyte at 1.6 V vs RHE (Figures 3c and S27). We observed a ca. 41 cm^{-1} negative shift in the $Co_{3-x}Ba_xO_4$ catalyst in the D_2O electrolyte, indicating the isotope exchange of H atoms by D atoms. Ba cation doping correlates thus with increased surface-adsorbed OH under acidic operating OER conditions.

To probe experimentally the OER mechanism, we used in situ synchrotron FT infrared (FTIR) spectroscopy under water oxidation conditions. The catalysts were dispersed on an Au/Si prism and assembled in an FTIR system. As shown in Figure 3d, a distinctive absorption peak at 1122 cm^{-1} was observed at 1.45 V vs RHE, suggesting the generation of an O−O bond, consistent with oxygen bridges between adjacent Co metal sites in the OPM mechanism.[32] Further FTIR studies under higher potentials revealed that this peak was positively shifted to 1136 cm^{-1}, something we assign to linearly-bonded superoxo species (M−O−O), which are the intermediate just prior to the release of O_2. When the potential was lowered again, the O−O and M−O−O bonds disappeared. We also conducted the in situ FTIR measurements on the Co_3O_4 catalysts (Figures 3e and S28).

We carried out isotope labeled operando differential electrochemical mass spectrometry (DEMS) to further prove the OPM mechanism (Figure S29). We used $H_2^{18}O$ and $H_2^{16}O$ as the supporting solution (0.5 M H_2SO_4). We detect the ^{32}O signal from the surface adsorbed ^{16}O coupling on neighboring Co sites when we report the OPM mechanism. As shown in the DEMS curves, we find that $Co_{3-x}Ba_xO_4$ steadily produced $^{32}O_2$, $^{34}O_2$, and $^{36}O_2$ at each LSV cycle. The Co_3O_4 only produced $^{34}O_2$ and $^{36}O_2$.

We summarize that Ba addition increases the Co valence state, shortens the M−M distance, and enriches OH adsorption. This agrees with prior reports that high-valence Co increases OH adsorption and produces a favorable local bonding environment.[33,34] We correlate the OPM pathway in $Co_{3-x}Ba_xO_4$ with the shorter M−M distance[32] and increased adsorbed OH[15], factors linked to O−O radical coupling and open coordination sites for O−O bond formation.

DFT Calculations. We sought to perform DFT calculations to gain insights into OER stability and activity on $Co_{3-x}Ba_xO_4$. We started by focusing on those surfaces of CoOOH as we characterized its presence in the FTIR spectra (Figure S30), which were generated in situ under OER conditions.[21,35,36] We calculated the surface free energies (Figure 4a,b) of these surfaces with vs without the presence of Ba dopants, on a variety of surface terminations (H-free (0001) surface of Co_3O_4/$Co_{3-x}Ba_xO_4$; ($01\bar{1}2$) surfaces with stoichiometry and 1 ML O_t of CoOOH/(Co,Ba)OOH; ($10\bar{1}4$) surfaces with stoichiometry and 1 ML H_2O of CoOOH/(Co,Ba)OOH). The calculated surfaces with surface-adsorbed Ba atoms are

summarized in Figure S31 with optimized geometries in Figures S32 and S33. This enabled us to contemplate the effect of Ba doping on the most thermodynamically stable surface and its relative stability under acidic water oxidation conditions (pH = 0−2 and U_{RHE} > 1.23 to ~1.7 V). For the CoOOH model, the ($10\bar{1}4$) surface with 1 ML H_2O is the most thermodynamically stable one when U_{RHE} < 2.15 V which originates from the fact that adsorption of H_2O[21] becomes energetically more favorable. The ($01\bar{1}2$) surface with 1 ML O_t becomes more stable when U_{RHE} > 2.15 V (Figure 4a). Without affecting the relative stability, surfaces with Ba-dopants result in more negative surface free energies, and their thermodynamic stabilities are thereby enhanced compared with those of pristine ones (Figure 4b), which agrees with the experimental trends. In the case of (Co,Ba)OOH, the ($10\bar{1}4$) surface with 1 ML H_2O retains the highest thermodynamic stability among the surfaces examined, the result of strong interactions between Ba and surface oxygens and hydroxides to form BaO_x; these are followed, in stability, by the ($01\bar{1}2$) surface with 1ML O_t.

After we identified the surface with the most thermodynamic stability, we performed further DFT calculations to investigate the origins of low overpotentials achieved using Ba doping. Predicted theoretical overpotentials (η_{theory}) versus the calculated Gibbs free energy differences between the formation of O* and OH* ($\Delta G_{O*} - \Delta G_{OH(I)*}$) are shown in the volcano plot of Figure 4c. The conventional AEM on the ($10\bar{1}4$) surface with 1 ML H_2O and ($01\bar{1}2$) surface with 1 ML O_t of CoOOH exhibit η_{theory} of 0.41 and 0.85 eV, respectively, showing that Co sites on the ($10\bar{1}4$) surface with 1 ML H_2O are the most active sites under acidic OER conditions.[37] We observed a significant reduction in η_{theory} after Ba doping, which we ascribed to the (1) migration of oxygen or hydroxide from Co sites (Figure S31) and (2) stabilization of μ−Co−OO−Co in vacant Co sites (Figure S34 and Table S6).[36] These electronic and geometric changes support an OPM mechanism that involves the coupling of two metal-oxo entities and the direct dissociation of O_2 (Figures 4d, S35).[37] The approach circumvents scaling relations among the OER intermediates in the AEM, enabling a low η_{theory} of 0.14 V on the ($10\bar{1}4$) surface with 1 ML H_2O on (Co,Ba)OOH, contributing to enhanced OER performance on (Co,Ba)OOH (predicted η_{theory} for the AEM are similar on CoOOH and (Co,Ba)OOH, more details in Table S6). These findings offer a possible account of the lower overpotential of $Co_{3-x}Ba_xO_4$ (278 mV at 10 mA/cm^2) achieved experimentally compared to the case of Co_3O_4.

■ CONCLUSIONS

Ba doping in a Co_3O_4 framework enables improved stability and enhanced catalytic performance during the OER. Experimental and DFT results suggest that the OPM mechanism on $Co_{3-x}Ba_xO_4$ exhibits faster water oxidation kinetics than does the AEM pathway on Co_3O_4 and that the lower surface free energy suggests improved stability in acidic electrolytes. The catalyst achieves an overpotential of 278 mV at 10 mA/cm^2 in acidic conditions for over 110 h of continuous operation.

■ ASSOCIATED CONTENT

Data Availability Statement

The data supporting this study are available in the paper and the Supplementary Information. All other relevant source data

are available from the corresponding authors upon reasonable request.

■ **Supporting Information**

The Supporting Information is available free of charge at https://pubs.acs.org/doi/10.1021/jacs.2c12431.

Experimental details, characterizations, and theoretical calculation details, figures of SEM images, XRD patterns, Refined XRD patterns, XPS spectra, HRTEM images, EDS mapping, in situ XANES and EXAFS spectra and fitting curves, in situ Raman and FTIR, ICP and DEMS, and tables of the calculation results and catalytic parameters (PDF)

■ **AUTHOR INFORMATION**

Corresponding Authors

    Hongyan Liang − *School of Materials Science and Engineering, Key Laboratory of Efficient Utilization of Low and Medium Grade Energy, Ministry of Education, Tianjin University, Tianjin 300350, P. R. China;* ⊙ orcid.org/0000-0001-6623-6946; Email: hongyan.liang@tju.edu.cn

    Edward H. Sargent − *Department of Electrical and Computer Engineering, University of Toronto, Toronto, Ontario M5S 1A4, Canada;* ⊙ orcid.org/0000-0003-0396-6495; Email: ted.sargent@utoronto.ca

Authors

    Ning Wang − *Department of Electrical and Computer Engineering, University of Toronto, Toronto, Ontario M5S 1A4, Canada; School of Materials Science and Engineering, Key Laboratory of Efficient Utilization of Low and Medium Grade Energy, Ministry of Education, Tianjin University, Tianjin 300350, P. R. China;* ⊙ orcid.org/0000-0002-2589-6881

    Pengfei Ou − *Department of Electrical and Computer Engineering, University of Toronto, Toronto, Ontario M5S 1A4, Canada;* ⊙ orcid.org/0000-0002-3630-0385

    Rui Kai Miao − *Department of Mechanical and Industrial Engineering, University of Toronto, Toronto, Ontario M5S 3G8, Canada*

    Yuxin Chang − *Department of Electrical and Computer Engineering, University of Toronto, Toronto, Ontario M5S 1A4, Canada*

    Ziyun Wang − *Department of Electrical and Computer Engineering, University of Toronto, Toronto, Ontario M5S 1A4, Canada; School of Chemical Sciences, The University of Auckland, Auckland 1010, New Zealand;* ⊙ orcid.org/0000-0002-2817-8367

    Sung-Fu Hung − *Department of Electrical and Computer Engineering, University of Toronto, Toronto, Ontario M5S 1A4, Canada; Department of Applied Chemistry, National Yang Ming Chiao Tung University, Hsinchu 300, Taiwan;* ⊙ orcid.org/0000-0002-7423-2723

    Jehad Abed − *Department of Electrical and Computer Engineering, University of Toronto, Toronto, Ontario M5S 1A4, Canada;* ⊙ orcid.org/0000-0003-1387-2740

    Adnan Ozden − *Department of Mechanical and Industrial Engineering, University of Toronto, Toronto, Ontario M5S 3G8, Canada;* ⊙ orcid.org/0000-0002-6924-1967

    Hsuan-Yu Chen − *Center for Condensed Matter Sciences and Center of Atomic Initiative for New Materials, National Taiwan University, Taipei 10617, Taiwan*

    Heng-Liang Wu − *Center for Condensed Matter Sciences and Center of Atomic Initiative for New Materials, National Taiwan University, Taipei 10617, Taiwan;* ⊙ orcid.org/0000-0003-1250-9851

    Jianan Erick Huang − *Department of Electrical and Computer Engineering, University of Toronto, Toronto, Ontario M5S 1A4, Canada*

    Daojin Zhou − *Department of Electrical and Computer Engineering, University of Toronto, Toronto, Ontario M5S 1A4, Canada*

    Weiyan Ni − *Department of Electrical and Computer Engineering, University of Toronto, Toronto, Ontario M5S 1A4, Canada*

    Lizhou Fan − *Department of Electrical and Computer Engineering, University of Toronto, Toronto, Ontario M5S 1A4, Canada*

    Yu Yan − *Department of Electrical and Computer Engineering, University of Toronto, Toronto, Ontario M5S 1A4, Canada*

    Tao Peng − *Department of Electrical and Computer Engineering, University of Toronto, Toronto, Ontario M5S 1A4, Canada;* ⊙ orcid.org/0000-0001-8517-5368

    David Sinton − *Department of Mechanical and Industrial Engineering, University of Toronto, Toronto, Ontario M5S 3G8, Canada*

    Yongchang Liu − *School of Materials Science and Engineering, Key Laboratory of Efficient Utilization of Low and Medium Grade Energy, Ministry of Education, Tianjin University, Tianjin 300350, P. R. China; State Key Lab of Hydraulic Engineering Simulation and Safety, School of Materials Science & Engineering, Tianjin University, Tianjin 300354, P.R. China*

Complete contact information is available at:
https://pubs.acs.org/10.1021/jacs.2c12431

Author Contributions

[†]N.W., P.O., R.K.M., Y.C., and Z.W. contributed equally to this work.

Notes

The authors declare no competing financial interest.

■ REFERENCES

(1) De Beer, F.; Van Der Merwe, J. H.; Bessarabov, D. PEM water electrolysis: preliminary investigations using neutron radiography. *Phys. Procedia* **2017**, *88*, 19–26.

(2) Pham, H. H.; Nguyen, N. P.; Do, C. L.; Le, B. T. Nanosized $Ir_xRu_{1-x}O_2$ electrocatalysts for oxygen evolution reaction in proton exchange membrane water electrolyzer. *Adv. Nat. Sci.: Nanosci. Nanotechnol.* **2015**, *6*, No. 025015.

(3) Oh, H. S.; Nong, H. N.; Reier, T.; Gliech, M.; Strasser, P. Oxide-supported Ir nanodendrites with high activity and durability for the oxygen evolution reaction in acid PEM water electrolyzers. *Chem. Sci.* **2015**, *6*, 3321–3328.

(4) Yao, Y.; Hu, S.; Chen, W.; Huang, Z.-Q.; Wei, W.; Yao, T.; Liu, R.; Zang, K.; Wang, X.; Wu, G.; Yuan, W.; Yuan, T.; Zhu, B.; Liu, W.; Li, Z.; He, D.; Xue, Z.; Wang, Y.; Zheng, X.; Dong, J.; Chang, C.-R.; Chen, Y.; Hong, X.; Luo, J.; Wei, S.; Li, W.-X.; Strasser, P.; Wu, Y.; Li, Y. Engineering the electronic structure of single atom Ru sites via compressive strain boosts acidic water oxidation electrocatalysis. *Nat. Catal.* **2019**, *2*, 304–313.

(5) Seitz, L. C.; Dickens, C. F.; Nishio, K.; Hikita, Y.; Montoya, J.; Doyle, A.; Kirk, C.; Vojvodic, A.; Hwang, H. Y.; Norskov, J. K.; Jaramillo, T. F. A highly active and stable $IrO_x/SrIrO_3$ catalyst for the oxygen evolution reaction. *Science* **2016**, *353*, 1011–1014.

(6) Han, N.; Yang, K. R.; Lu, Z.; Li, Y.; Xu, W.; Gao, T.; Cai, Z.; Zhang, Y.; Batista, V. S.; Liu, W.; Sun, X. Nitrogen-doped tungsten carbide nanoarray as an efficient bifunctional electrocatalyst for water splitting in acid. *Nat. Commun.* **2018**, *9*, 924.

(7) Chatti, M.; Gardiner, J. L.; Fournier, M.; Johannessen, B.; Williams, T.; Gengenbach, T. R.; Pai, N.; Nguyen, C.; MacFarlane, D. R.; Hocking, R. K.; Simonov, A. N. Intrinsically stable in situ generated electrocatalyst for long-term oxidation of acidic water at up to 80 °C. *Nat. Catal.* **2019**, *2*, 457–465.

(8) Reier, T.; Nong, H. N.; Teschner, D.; Schlögl, R.; Strasser, P. Electrocatalytic oxygen evolution reaction in acidic environments - reaction mechanisms and catalysts. *Adv. Energy Mater.* **2017**, *7*, No. 1601275.

(9) Wen, Y.; Liu, C.; Huang, R.; Zhang, H.; Li, X.; Garcia de Arquer, F. P.; Liu, Z.; Li, Y.; Zhang, B. Introducing Bronsted acid sites to accelerate the bridging-oxygen-assisted deprotonation in acidic water oxidation. *Nat. Commun.* **2022**, *13*, 4871.

(10) Spöri, C.; Briois, P.; Nong, H. N.; Reier, T.; Billard, A.; Kühl, S.; Teschner, D.; Strasser, P. Experimental activity descriptors for Iridium-based catalysts for the electrochemical oxygen evolution reaction (OER). *ACS Catal.* **2019**, *9*, 6653–6663.

(11) Pi, Y.; Shao, Q.; Wang, P.; Guo, J.; Huang, X. General formation of monodisperse IrM (M = Ni, Co, Fe) bimetallic nanoclusters as bifunctional electrocatalysts for acidic overall water splitting. *Adv. Funct. Mater.* **2017**, *27*, No. 1700886.

(12) Plaisance, C. P.; Reuter, K.; Van Santen, R. A. Quantum chemistry of the oxygen evolution reaction on cobalt(ii,iii) oxide - implications for designing the optimal catalyst. *Faraday Discuss.* **2016**, *188*, 199–226.

(13) Wang, L.-P.; Van Voorhis, T. Direct-coupling O_2 bond forming a pathway in cobalt oxide water oxidation catalysts. *J. Phys. Chem. Lett.* **2011**, *2*, 2200–2204.

(14) Plaisance, C. P.; Van Santen, R. A. Structure sensitivity of the oxygen evolution reaction catalyzed by cobalt (II, III) oxide. *J. Am. Chem. Soc.* **2015**, *137*, 14660–14672.

(15) Ullman, A. M.; Brodsky, C. N.; Li, N.; Zheng, S.-L.; Nocera, D. G. Probing edge site reactivity of oxidic cobalt water oxidation catalysts. *J. Am. Chem. Soc.* **2016**, *138*, 4229–4236.

(16) Wang, H. Y.; Hung, S. F.; Hsu, Y. Y.; Zhang, L.; Miao, J.; Chan, T. S.; Xiong, Q.; Liu, B. In situ spectroscopic identification of mu-OO bridging on spinel Co_3O_4 water oxidation electrocatalyst. *J. Phys. Chem. Lett.* **2016**, *7*, 4847–4853.

(17) Huang, J.; Sheng, H.; Ross, R. D.; Han, J.; Wang, X.; Song, B.; Jin, S. Modifying redox properties and local bonding of Co_3O_4 by CeO_2 enhances oxygen evolution catalysis in acid. *Nat. Commun.* **2021**, *12*, 3036.

(18) Yu, J.; Garces-Pineda, F. A.; Gonzalez-Cobos, J.; Pena-Diaz, M.; Rogero, C.; Gimenez, S.; Spadaro, M. C.; Arbiol, J.; Barja, S.; Galan-Mascaros, J. R. Sustainable oxygen evolution electrocatalysis in aqueous 1 M H_2SO_4 with earth abundant, nanostructured Co_3O_4. *Nat. Commun.* **2022**, *13*, 4341.

(19) Yan, K.-L.; Qin, J.-F.; Lin, J.-H.; Dong, B.; Chi, J.-Q.; Liu, Z.-Z.; Dai, F.-N.; Chai, Y.-M.; Liu, C.-G. Probing the active sites of Co_3O_4 for the acidic oxygen evolution reaction by modulating the Co^{2+}/Co^{3+} ratio. *J. Mater. Chem. A* **2018**, *6*, 5678–5686.

(20) Mondschein, J. S.; Callejas, J. F.; Read, C. G.; Chen, J. Y. C.; Holder, C. F.; Badding, C. K.; Schaak, R. E. Crystalline cobalt oxide films for sustained electrocatalytic oxygen evolution under strongly acidic conditions. *Chem. Mater.* **2017**, *29*, 950–957.

(21) Bajdich, M.; Garcia-Mota, M.; Vojvodic, A.; Norskov, J. K.; Bell, A. T. Theoretical investigation of the activity of cobalt oxides for the electrochemical oxidation of water. *J. Am. Chem. Soc.* **2013**, *135*, 13521–13530.

(22) Huang, W.; Li, J.; Liao, X.; Lu, R.; Ling, C.; Liu, X.; Meng, J.; Qu, L.; Lin, M.; Hong, X.; Zhou, X.; Liu, S.; Zhao, Y.; Zhou, L.; Mai, L. Ligand modulation of active sites to promote electrocatalytic oxygen evolution. *Adv. Mater.* **2022**, *34*, No. 2200270.

(23) Yang, X.; Li, H.; Lu, A.-Y.; Min, S.; Idriss, Z.; Hedhili, M. N.; Huang, K.-W.; Idriss, H.; Li, L.-J. Highly acid-durable carbon coated Co_3O_4 nanoarrays as efficient oxygen evolution electrocatalysts. *Nano Energy* **2016**, *25*, 42–50.

(24) Blasco-Ahicart, M.; Soriano-Lopez, J.; Carbo, J. J.; Poblet, J. M.; Galan-Mascaros, J. R. Polyoxometalate electrocatalysts based on earth-abundant metals for efficient water oxidation in acidic media. *Nat. Chem.* **2018**, *10*, 24–30.

(25) Hibberd, A. M.; Doan, H. Q.; Glass, E. N.; de Groot, F. M. F.; Hill, C. L.; Cuk, T. Co polyoxometalates and a Co_3O_4 thin film investigated by L-edge X-ray absorption spectroscopy. *J. Phys. Chem. C* **2015**, *119*, 4173–4179.

(26) Wang, H. Y.; Hung, S. F.; Chen, H. Y.; Chan, T. S.; Chen, H. M.; Liu, B. In operando identification of geometrical-site-dependent water oxidation activity of spinel Co_3O_4. *J. Am. Chem. Soc.* **2016**, *138*, 36–39.

(27) Han, M.; Wang, N.; Zhang, B.; Xia, Y.; Li, J.; Han, J.; Yao, K.; Gao, C.; He, C.; Liu, Y.; Liang, H. Y. High-valent nickel promoted by atomically embedded copper for efficient water oxidation. *ACS Catal.* **2020**, *10*, 9725–9734.

(28) Görlin, M.; Chernev, P.; Ferreira de Araújo, J.; Reier, T.; Dresp, S.; Paul, B.; Krähnert, R.; Dau, H.; Strasser, P. Oxygen evolution reaction dynamics, faradaic charge efficiency, and the active metal redox states of Ni—Fe oxide water splitting electrocatalysts. *J. Am. Chem. Soc.* **2016**, *138*, 5603–5614.

(29) Long, X.; Yu, P.; Zhang, N.; Li, C.; Feng, X.; Ren, G.; Zheng, S.; Fu, J.; Cheng, F.; Liu, X. Direct Spectroscopy for probing the critical role of partial covalency in oxygen reduction reaction for cobalt-manganese spinel oxides. *Nanomaterials* **2019**, *9*, 577.

(30) Chen, D.; Zhong, J.; Wu, X.; Wu, Z.; Mironova-Ulmane, N.; Kuzmin, A.; Marcelli, A. Oxygen K-edge XANES investigation of $Ni_cMg_{1-c}O$ solid solutions. *Spectrochim. Acta, Part A* **2008**, *70*, 458–461.

(31) Guo, Z.; Ye, W.; Fang, X.; Wan, J.; Ye, Y.; Dong, Y.; Cao, D.; Yan, D. Amorphous cobalt—iron hydroxides as high-efficiency oxygen-evolution catalysts based on a facile electrospinning process. *Inorg. Chem. Front.* **2019**, *6*, 687–693.

(32) Lin, C.; Li, J.-L.; Li, X.; Yang, S.; Luo, W.; Zhang, Y.; Kim, S.-H.; Kim, D.-H.; Shinde, S. S.; Li, Y.-F.; Liu, Z.-P.; Jiang, Z.; Lee, J.-H. In-situ reconstructed Ru atom array on α-MnO$_2$ with enhanced performance for acidic water oxidation. *Nat. Catal.* **2021**, *4*, 1012–1023.

(33) Zheng, X.; Zhang, B.; Luna, P. D.; Liang, Y.; Comin, R.; Voznyy, O.; Han, L.; Arquer, F. P. G.; Liu, M.; Dinh, C. T.; Sargent,

E. H. Theory-driven design of high-valence metal sites for water oxidation confirmed using in situ soft X-ray absorption. *Nat. Chem.* **2018**, *10*, 149−154.

(34) Cao, L.; Luo, Q.; Liu, W.; Lin, Y.; Liu, X.; Cao, Y.; Zhang, W.; Wu, Y.; Yang, J.; Yao, T.; Wei, S. Identification of single-atom active sites in carbon-based cobalt catalysts during electrocatalytic hydrogen evolution. *Nat. Catal.* **2019**, *2*, 134−141.

(35) Curutchet, A.; Colinet, P.; Michel, C.; Steinmann, S. N.; Le Bahers, T. Two-sites are better than one: revisiting the OER mechanism on CoOOH by DFT with electrode polarization. *Phys. Chem. Chem. Phys.* **2020**, *22*, 7031−7038.

(36) Zhang, B.; Zheng, X.; Voznyy, O.; Comin, R.; Bajdich, M.; Garcia-Melchor, M.; Han, L.; Xu, J.; Liu, M.; Zheng, L.; Garcia de Arquer, F. P.; Dinh, C. T.; Fan, F.; Yuan, M.; Yassitepe, E.; Chen, N.; Regier, T.; Liu, P.; Li, Y.; De Luna, P.; Janmohamed, A.; Xin, H. L.; Yang, H.; Vojvodic, A.; Sargent, E. H. Homogeneously dispersed multimetal oxygen-evolving catalysts. *Science* **2016**, *352*, 333−337.

(37) Craig, M. J.; Coulter, G.; Dolan, E.; Soriano-López, J.; Mates-Torres, E.; Schmitt, W.; García-Melchor, M. Universal scaling relations for the rational design of molecular water oxidation catalysts with near-zero overpotential. *Nat. Commun.* **2019**, *10*, 4993.